Supplemental material: Shear flow as a tool to distinguish microscopic activities of molecular machines in a chromatin loop

Sandeep Kumar[1], Ranjith Padinhateeri[2], and Snigdha Thakur[1]

[1]Indian Institute of Science Education and Research, Bhopal-462066
[2]Indian Institute of Technology Bombay, Mumbai-400076

S1 Model and Simulation Details

We consider an isolated flexible ring polymer of size $N = 200$, which is subjected to simple shear flow. Neighboring monomers are connected by harmonic spring potential, which is defined as :

$$U_h = \frac{1}{2}\kappa(r_{ij} - l_0)^2 \tag{1}$$

where, κ is the spring constant and l_0 is the equilibrium separation between the monomers. The non-neighboring monomers interact via purely repulsive L-J potential (WCA) to prevent overlap between them.

$$U_{LJ} = \begin{cases} 4\epsilon\left[\left(\frac{\sigma}{r}\right)^{12} - \left(\frac{\sigma}{r}\right)^{6} + \frac{1}{4}\right] & \text{for } r = |\mathbf{r}_i - \mathbf{r}_j| < 2^{\frac{1}{6}}\sigma \\ 0 & otherwise \end{cases} \tag{2}$$

Here, ϵ is the strength of the repulsion and σ is the diameter of each monomer.

To include activity on the polymer we apply two types of tangential force on the polymer. In type-I activity, a tangential force is applied using the following definition:

$$\mathbf{F}_a^{\textit{type-I}} = f_t\hat{\mathbf{t}}. \tag{3}$$

where $\hat{\mathbf{t}} = (\mathbf{r}_{i+1} - \mathbf{r}_{i-1})/\mid \mathbf{r}_{i+1} - \mathbf{r}_{i-1} \mid$ is the unit vector along the tangent to the backbone of i^{th} monomer. It is to be noted that in equation(3), i.e. in type-I activity, the magnitude of active force remains constant irrespective of the shape fluctuations of the polymer contour because the force is applied along the unit vector. In a separate set of simulations, we adopt another form of the active force defined as :

$$\mathbf{F}_a^{\,type\text{-}II} = f_t \mathbf{t}. \tag{4}$$

$\mathbf{t}_i = (\mathbf{r}_{i+1} - \mathbf{r}_{i-1})/2l$, where $l = \mid \mathbf{r}_{i+1} - \mathbf{r}_i \mid$ is the bond length. Note that type-II activity constitutes the active force that is affected by the local curvature along the contour.

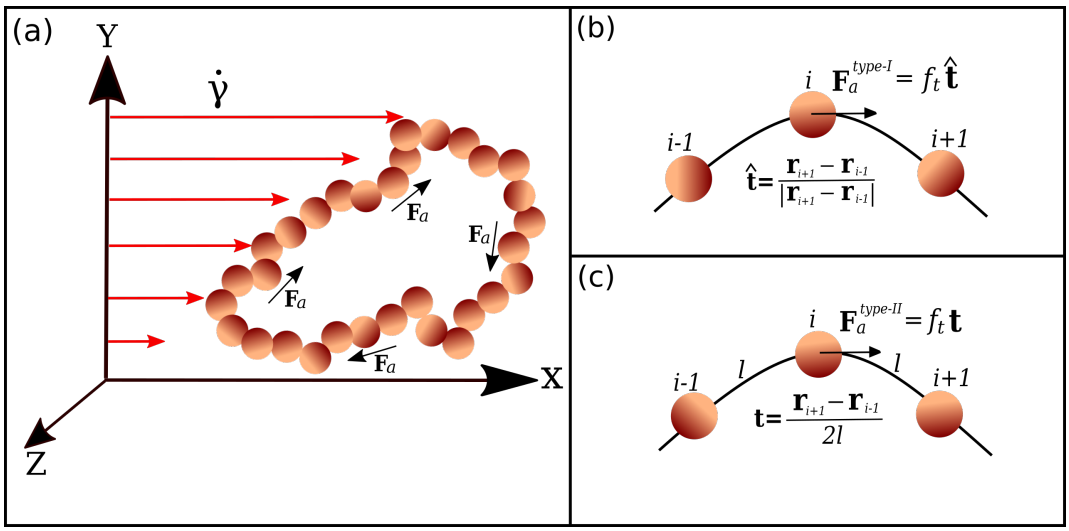

Figure S1: This is the reproduction of Figure 1 of the main text, showing the schematic representation of the active ring under the shear flow.

Fig. S1 shows the schematic representation of our active ring polymer subjected to simple shear flow along the x-direction. Because of the shear flow, the velocity field is modified by a velocity gradient tensor given by : $\nabla \mathbf{u} = \begin{pmatrix} 0 & \dot{\gamma} & 0 \\ 0 & 0 & 0 \\ 0 & 0 & 0 \end{pmatrix}$, $\dot{\gamma} = \frac{du_x}{dy}$ is the constant shear rate. Therefore, for each i^{th} bead the equation of motion is given:

$$m\ddot{\mathbf{r}}_i = -\nabla U_i + \mathbf{F}_s^i + \mathbf{F}_a^i - \beta \dot{\mathbf{r}}_i + \boldsymbol{\xi}_i \tag{5}$$

$\mathbf{F_s} = \beta \nabla \mathbf{u} \cdot \mathbf{r}$ is the force due to shear flow, $\mathbf{F}_a$ is the active force, β is the friction coefficient and $\boldsymbol{\xi}$ is the Gaussian white noise with zero mean and unit variance and satisfies the relation $\langle \boldsymbol{\xi}_i(t_1) \cdot \boldsymbol{\xi}_j(t_2) \rangle = \sqrt{6\beta k_B T}\delta_{ij}\delta(t_1 - t_2)$.

The strength of the activity is measured by the activity number $Ac = \frac{f_t \sigma}{K_B T}$. To distinguish between the two forms of active force, we use $Ac\text{-}I$ and $Ac\text{-}II$ to measure the activity strength for type-I and type-II rings, respectively. Apart from that, we use the well-known quantity called Weissenberg number (Wi) to account for the strength of the shear flow. $Wi = \dot{\gamma}\tau_0$, where τ_0 is the longest relaxation time of the passive ring without shear. To calculate τ_0, we start from the maximum extended configuration of the ring polymer in the x-direction, for which the fractional extension $\Delta x/L \approx 0.5$, and let the system evolve without shear and active force. The ratio $\Delta x/L$ decays with time until it reaches saturation. We fit the tail

end of the decay (when $\Delta x/L \leq 0.2$) with the expression $(\Delta x/L)^2 = Aexp(-t/\tau_0) + B$ to obtain the longest relaxation time $\tau_0 \approx 7500$.

Simulation Parameters: In the present study, the ring polymer is placed near the centre of a cubic box of size $200 \times 200 \times 200$. All simulations are performed at a constant temperature of the thermal bath with $K_BT = 0.1$ and $\epsilon = 0.1$. The equilibrium separation between monomers is $l_0 = 1.25\sigma$, where $\sigma = 2$ is the diameter of each bead. The spring constant κ has been taken to be $250, 1000, 3000$ depending on the shear rate to keep l_0 fixed. To evolve the system, we integrate the equation of motion using the velocity-Verlet scheme in steps of $dt = 10^{-3}$ and $dt = 5 \times 10^{-4}$. The polymer is allowed to relax under shear flow for more than $10 \times \tau_0$, in more than 40 independent sets of simulations. Shear is applied to the system using Lees-Edwards boundary conditions.

S2 Structural analysis

In Fig. S2(a), we show the effect of type-I and type-II active force on polymer size in the absence of shear. Without shear, both kinds of activity eventually lead to the collapsed state of the ring. However, a higher magnitude of activity is required to trigger the collapse in type-II ($Ac\text{-}II = 10$ onwards) than type-I ($Ac\text{-}I = 5$ onwards). Once the globular state is reached, the gyration radius remains similar in both cases (Fig. S2(a)). As shown in our previous study [2], the collapse of the ring is due to the formation of local hairpin-like structures. In Fig. S2(b), we plot the bond-correlation function defined as $\beta(s) = \langle \mathbf{b}_{i+s} \cdot \mathbf{b}_i \rangle$, where $\mathbf{b}_i = \mathbf{r}_{i+1} - \mathbf{r}_i$ is the bond vector. The negative minimum in $\beta(s)$ is a signature of such local hairpin structures, which are present in $Ac\text{-}I \geq 5$ and $Ac\text{-}II \geq 10$. Further, it is also observed in Fig. S2(c) that $\mathbf{F}_a^{type-II}$ takes a longer time to collapse the ring as compared to $\mathbf{F}_a^{type-I}$.

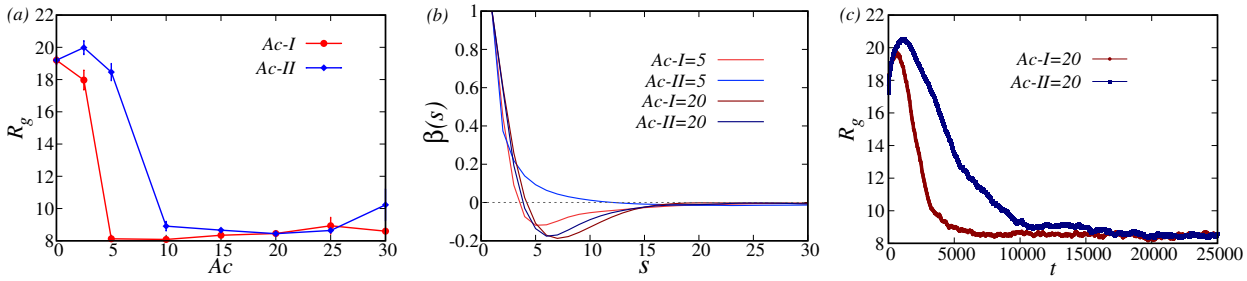

Figure S2: (a) Comparison of polymer compaction for the two kinds of active forces without shear ($Wi = 0$). (b) Bond correlation of type-I and type-II active ring without shear($Wi = 0$). (c) R_g vs t for $Wi = 0$ case showing faster collapse in type-I active ring.

The gyration tensor (G_{mn}) analysis of the ring in the presence of shear flow shows a considerably distinct effect of the kind of microscopic activity on the polymer structure. In Fig. S3, we show the scaled diagonal elements of the gyration tensor, $3G_{xx}/R_{g0}^2$, $3G_{yy}/R_{g0}^2$

and $3G_{zz}/R^2_{g0}$ where R^2_{g0} is the square of gyration radius without shear. Passive ring polymers show a steady rise in G_{xx} with increasing Wi as they get stretched in the flow direction. This elongation in the x-direction occurs at the expense of the polymer's compaction along the gradient (y) and vorticity (z) direction, as seen in Fig. S3(b) and (c). The type-II ring displays a similar behaviour of G_{mm} as that of passive with a small deviation for lower Wi. However, type-I rings show a sudden transition from globular to completely extended state with G_{xx} saturating after $Wi \approx 150$. In the gradient direction, G_{yy} also displays a small region of non-monotonicity at low Wi. In this region, the globular ring polymer unfolds steadily, thereby increasing G_{yy} and reaching a maximum value. Further increasing Wi leads to compaction along the y-direction, and G_{yy} decreases as G_{xx} increases rapidly. Interestingly, we observe a swelling of type-II ring polymer in the vorticity direction compared to type-I shown in the G_{zz} plot.

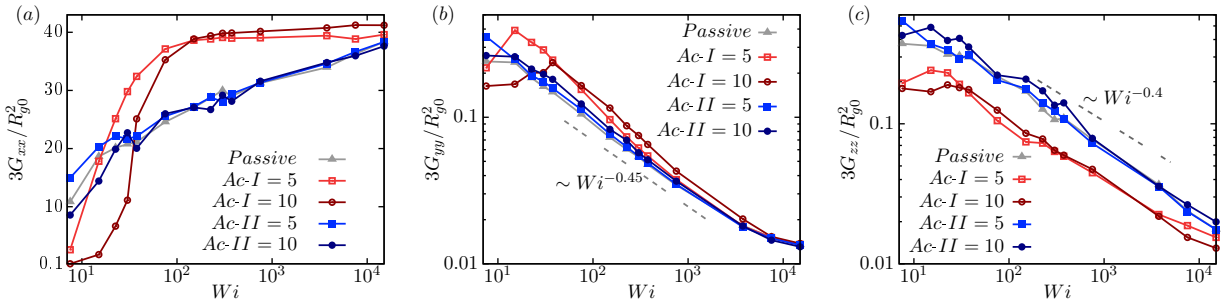

Figure S3: G_{xx}, G_{yy} and G_{zz} as a function of Wi for both kind of tangential activity.

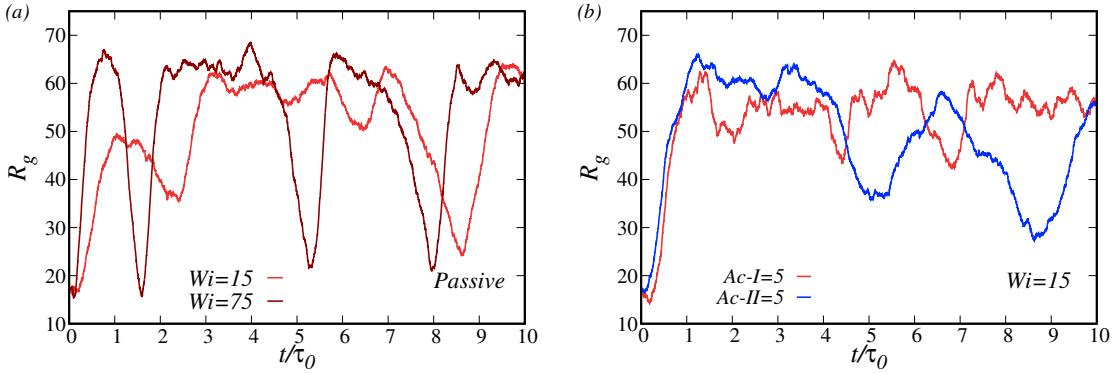

Figure S4: Time evolution of R_g for passive and $Ac\text{-}I, Ac\text{-}II = 5$.

In Fig. S4 and Fig. S5, we present the time series of R_g, which has been used to calculate probability distribution ($P(R_g)$) in the main text as well as in Fig. S6 and Fig. S7. The passive ring in Fig. S4(a) spans a wide range of R_g values, which leads to a broad distribution of $P(R_g)$. Distinct open and closed states for type-I activity are also visible here. For $Ac\text{-}I = 10$, the ring remains in the globular state at $Wi = 15$ and stretches completely

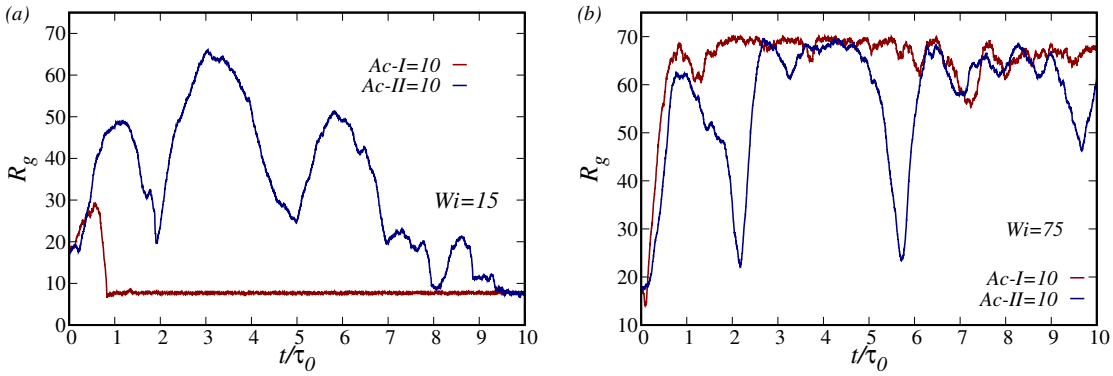

Figure S5: Time evolution of R_g for $Ac\text{-}I, Ac\text{-}II = 10$ at $Wi = 15$ and 75.

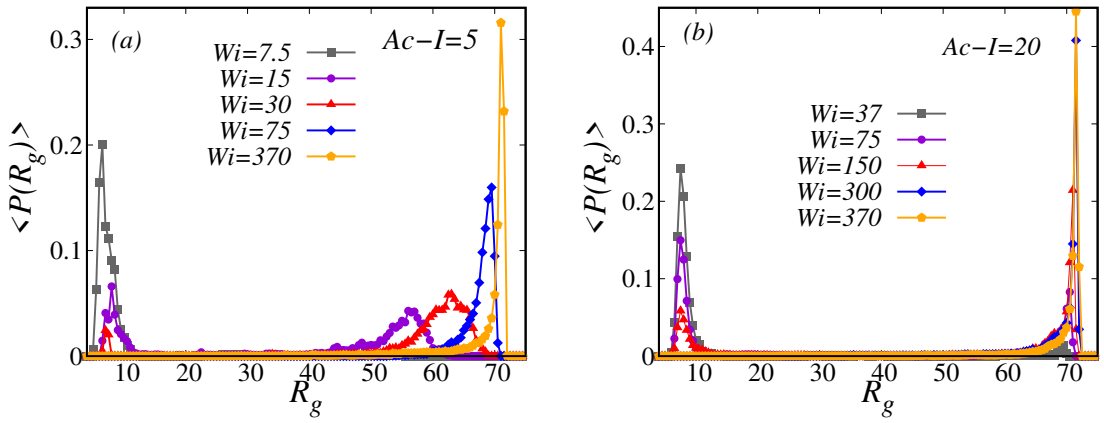

Figure S6: Distribution of R_g for $Ac\text{-}I = 5$ and 20 at different Wi values.

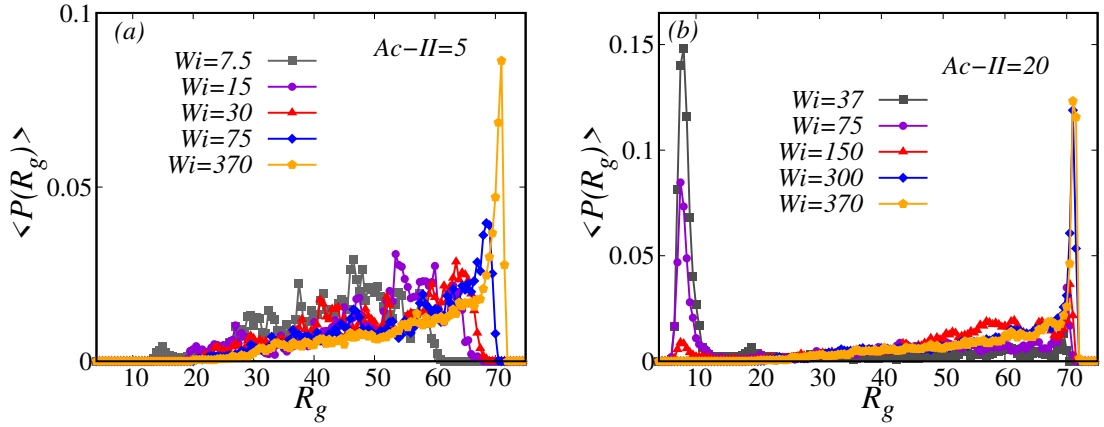

Figure S7: Distribution of R_g for $Ac\text{-}II = 5$ and 20 at different Wi values.

at $Wi = 75$. It should be noted that type-I remains very stable in either collapsed or stretched configurations, which gives rise to a bimodal distribution of R_g. This feature is absent in type-II rings, which makes a smooth transition between compact and elongated

states. In the subsequent figures (Fig. S6 and Fig. S7) we present the $P(R_g)$ for $Ac\text{-}I = 5, 20$ and $Ac\text{-}II = 5, 20$, which shows similar features as discussed above. We also calculate the standard deviation of the probability distribution $P(R_g)$ as $\sigma(R_g) = \sqrt{\sum_{i=1}^{n}(R_g^i - \langle R_g \rangle)^2/n}$, which is shown in the main text. The binder cumulant for R_g distribution is defined as $BC = 1 - \frac{\langle R_g^4 \rangle}{3\langle R_g^2 \rangle^2}$ and has been discussed in the main text.

S3 Tumbling Properties

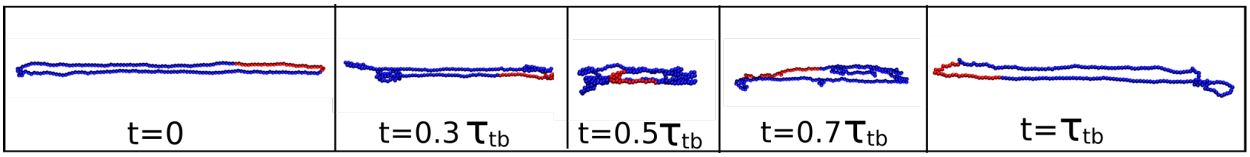

Figure S8: Snapshot of an active ring polymer showing tumbling motion at $Wi = 370$. Time is denoted in increasing order from $t = 0$ to $t = \tau_{tb}$. The red segment in the ring is for visual aid.

Snapshots of a complete tumbling event are shown in Fig. S8. The polymer undergoes one tumbling cycle in time interval $t = 0$ to $t = \tau_{tb}$, where τ_{tb} is the characteristic tumbling time. As discussed in the main text, the characteristic tumbling time τ_{tb} as well as tumbling frequency f_{tb} can be obtained from the cross-correlation function given as:

$$C_{xy}(t) = \frac{\langle \delta G_{xx}(t_0)\delta G_{yy}(t_0 + t)\rangle}{\langle \delta G_{xx}^2(t_0)\rangle \langle \delta G_{yy}^2(t_0)\rangle} \tag{6}$$

where, $G_{\alpha\alpha}$ are elements of the gyration tensor and $\delta G_{\alpha\alpha} = G_{\alpha\alpha} - \langle G_{\alpha\alpha}\rangle$ and $\delta G_{\alpha\alpha}^2 = \langle G_{\alpha\alpha}^2\rangle - \langle G_{\alpha\alpha}\rangle^2$. In Fig. S9, we report the C_{xy}(t) as a function of time for passive, $Ac\text{-}I = 10$

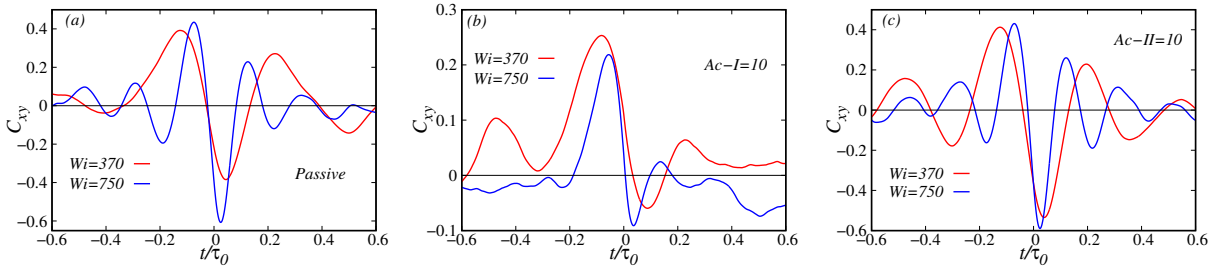

Figure S9: Cross-correlation (C_{xy}) of the fluctuations in G_{xx} and G_{yy} for passive, $Ac\text{-}I = 10$ and $Ac\text{-}II = 10$ case.

and $Ac\text{-}II = 10$, which is then utilized to calculate the tumbling frequency f_{tb} as defined in the main text. As discussed there, f_{tb} shows similar scaling in type-I and type-II rings; however, it is clear from Fig. S9 that the amplitudes of C_{xy} in type-I rings are much smaller as compared to passive and type-II rings. The amplitude can be related to the smoothness

of tumbling. We quantify the smoothness from the height of the positive and negative peaks and define it as $Q_{tb} = C^{+}_{xy} - C^{-}_{xy}$, where C^{+}_{xy} and C^{-}_{xy} are the heights of positive and negative peaks of C_{xy} respectively. Q_{tb} shown in Fig. S10 is observed to be higher in passive and type-II rings as compared to type-I rings. The C_{xy} plot, along with their Q_{tb} values, suggest that the tumbling events are less smooth in the case of type-I, i.e. the constant active force case. Here, the active force always tries to reduce the fluctuations in the polymer size along the gradient direction, which in turn makes δG_{yy} small. Although this mechanism does not affect the tumbling frequency, rather it makes the tumbling events less smooth. On the other hand, when activity varies according to the local shape of the polymer backbone (type-II), those random fluctuations (δG_{yy}) are sustained, which consequently leads to very clear tumbling events.

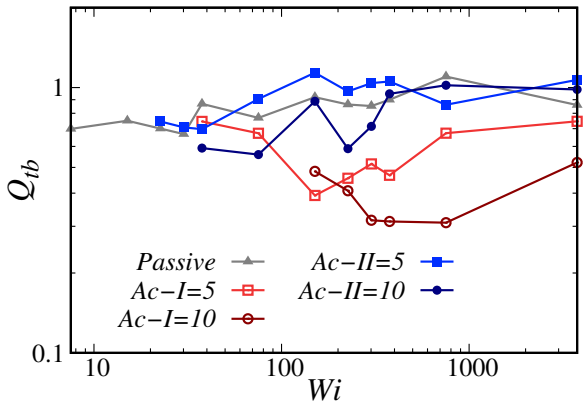

Figure S10: Smoothness of tumbling Q_{tb} for the two case of tangential activity.

S4 Tank-Treading Properties

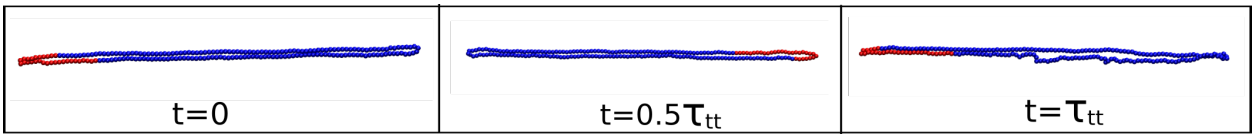

Figure S11: A representative snapshot of an active ring polymer showing Tank-treading motion. Time is denoted in increasing order from $t = 0$ to $t = \tau_{tt}$. The red segment in the ring is for visual aid.

Ring polymers subjected to shear flow show a peculiar motion known as tank-treading (TT), in which the ring maintains its shape and rotates steadily about its centre of mass. TT motion occurs when the polymer is completely stretched in the flow-gradient plane with a high-velocity gradient across monomers. In Fig. S11, we show the snapshots of an active ring undergoing a complete tank-treading cycle. As evident from the snapshots, the segment coloured in red moves from the left side (at $t = 0$) to the right side (at $t = 0.5\tau_{tt}$) and

again comes back to the left side after completing the complete TT cycle (at $t = \tau_{tt}$). To comprehend the TT cycle's characteristic time or frequency, we track a monomer's motion in the following way. For a given bead i, we define $X_i = x_i/L$, where $x_i = (\mathbf{r}_i - \mathbf{r}_{cm})_x$ is the x-position of i^{th} monomer in the centre of mass (r_{cm}) reference frame and L is the distance between the extreme beads along the longitudinal axis of the ring. A pictorial representation of x_i and L is given in Fig. S12.

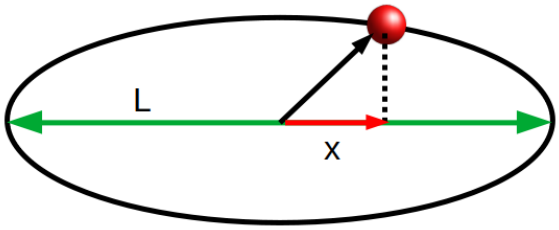

Figure S12: Pictorial representation of the longitudinal axis L shown in green. $\mathbf{x}$ is the projection of an arbitrary monomer's position on the longitudinal axis.

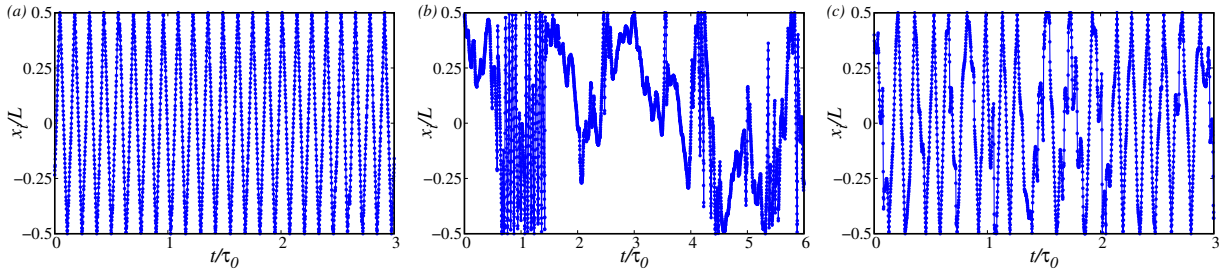

Figure S13: Variation of x_i/L for $Ac\text{-}I = 5$ at $Wi = 370, 3700$ & 7500

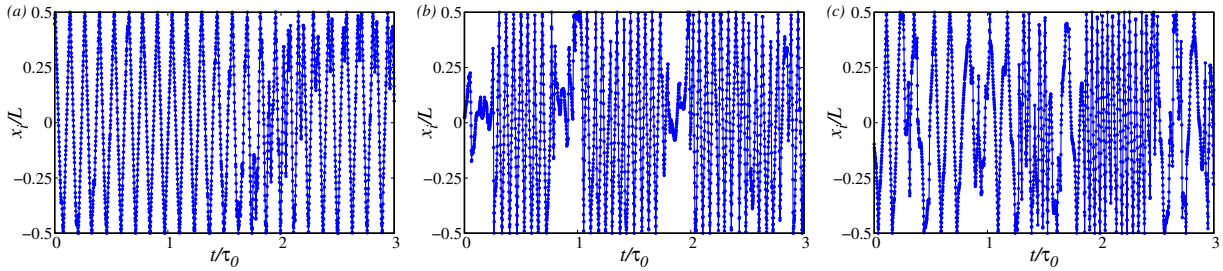

Figure S14: Variation of x_i/L for $Ac\text{-}II = 5$ at $Wi = 370, 3700$ & 7500.

Fig. S13 shows the variation of x_i/L for $Ac\text{-}I = 5$ at three different Wi values. At $Wi = 370$, X_i displays a nice oscillatory behaviour with time as the monomers move along the elliptical path on the contour during the TT cycle (Fig. S13(a)). However, as we increase Wi to 3700

(Fig. S13(b)), competition between the constant active force and shear flow begins to appear, and the TT motion slows down. This phenomenon is evident from the irregular oscillation in X_i in Fig. S13(b). Upon further increasing the Wi, shear dominates the activity, and TT motion is restored. In contrast, for $Ac\text{-}II = 5$ shown in Fig. S14, this competition between the active force and shear is hugely suppressed, and the ring exhibits TT motion at all values of Wi.

We define the time auto-correlation of the fraction x_i/L as:

$$C_{x_i/L}(t) = \frac{\langle X_i(t_0)X_i(t_0+t)\rangle}{\langle X_i^2(t_0)\rangle} \tag{7}$$

and plot it in Fig. S15. The secondary peak in the plot of $C_{x_i/L}(t)$ is used to identify τ_{tt},

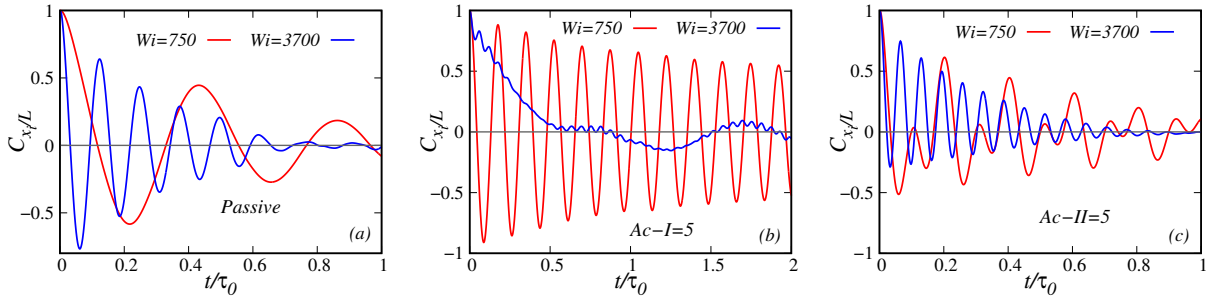

Figure S15: $C_{x/L}$ for passive, $Ac\text{-}I = 5$ and $Ac\text{-}II = 5$ case.

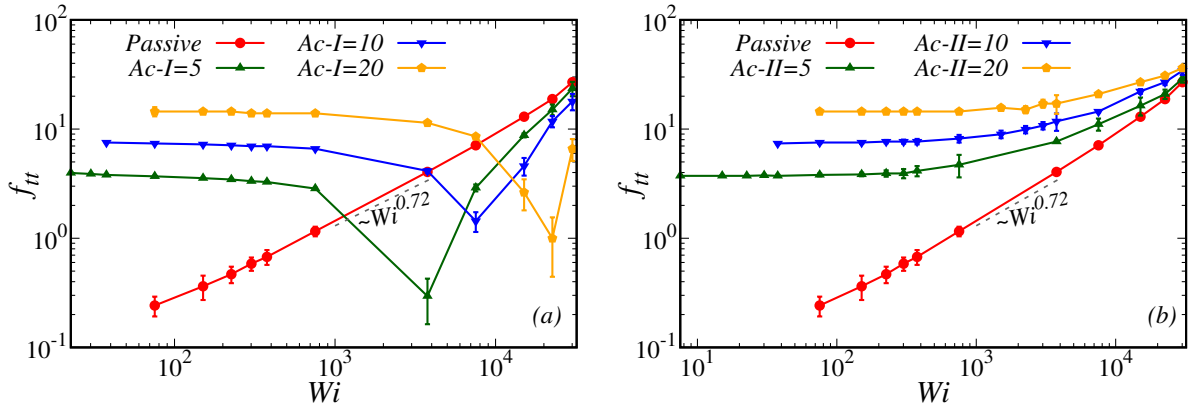

Figure S16: Scaled tank-treading frequency for type-I and type-II active rings at different Wi obtained from $C_{x/L}$.

which is the characteristic time of tank-treading motion. We obtain scaled tank-treading frequency $f_{tt} = \tau_0/\tau_{tt}$. In Fig. S15, we report the $C_{x_i/L}$ for passive, $Ac\text{-}I = 5$ and $Ac\text{-}II = 5$ at two different Wi. The corresponding tank-treading frequency for type-I and type-II active rings has been shown separately in Fig. S16. For the passive ring, f_{tt} increases monotonically with an increase in Wi following a power law scaling of $\sim Wi^{0.72}$.

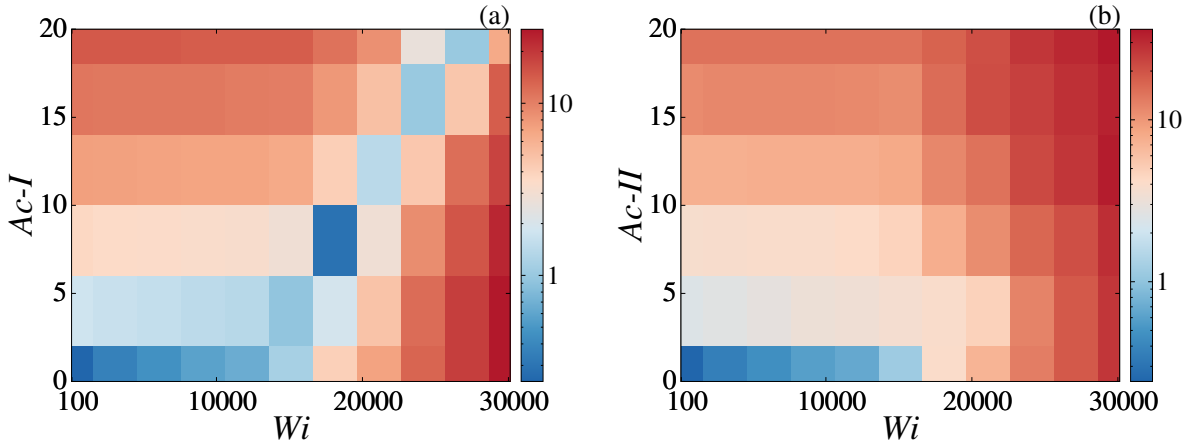

Figure S17: Phase diagram of the tank-treading frequencies (f_{tt}) for different values of Wi and activity strength. The values of the colour gradient represent numerically the scaled f_{tt} in (a) type-I and (b) type-II active rings.

On the other hand, the active rings show a completely different response in TT frequency when Wi is increased. It is noteworthy that, unlike the passive case, the active ring at lower Wi exhibits a plateau in the tank-treading frequency f_{tt} whose magnitude increases with activity strength. This is due to the fact that the tangential active force alone can drive the ring monomers into the TT motion. Therefore, for smaller Wi, the observed TT is dominated by the active forces. Interestingly, at the intermediate Wi, the type-I and type-II exhibit a completely different trend in f_{tt}. As discussed in the main text, type-I ring experiences a competition between the active tangential force and the shear force that impacts their TT motion. With the increase in Wi, this competition becomes substantial, and f_{tt} starts decreasing until it reaches a minimum. To understand this minimum, please refer to (Fig. S15(b)). One can see that at $Wi \approx 3700$, the oscillations in $C_{x_i/L}$ are feeble compared to $Wi \approx 750$, indicating the stalling of the TT motion. Such stalling is not observed for type-II activity. To summarize the distinct tank-treading properties of the two activities, we have added a phase diagram of f_{tt} at different Wi and Ac for both activities.

S5 Simulation including hydrodynamic interactions

The above proposed model does not include any hydrodynamic interaction (HI) that may have a role to play in real systems. To check the robustness of shear to act as a tool to differentiate the activities even in the presence of HI, we perform Brownian dynamics simulations, including hydrodynamic interactions. In the implicit solvent method, hydrodynamics is approximated via a configuration-dependent diffusion coefficient tensor. We represent the

diffusion tensor by the Rotne-Prager-Yamakawa (RPY) tensor, which takes the form [5, 4]:

$$D_{ij} = \begin{cases} \left(\frac{k_B T}{6\pi\eta a}\right)\mathbf{I} & \text{for } i = j \\ \left(\frac{k_B T}{8\pi\eta r_{ij}}\right)\left[\left(1+\frac{2a^2}{3r_{ij}^2}\right)\mathbf{I} + \left(1-\frac{2a^2}{r_{ij}^2}\frac{\mathbf{r}_{ij}\mathbf{r}_{ij}}{r_{ij}^2}\right)\right] & \text{for } i \neq j \text{ and } r_{ij} \geq 2a \\ \left(\frac{k_B T}{6\pi\eta a}\right)\left[\left(1-\frac{9r_{ij}}{32a}\right)\mathbf{I} + \frac{3\mathbf{r}_{ij}\mathbf{r}_{ij}}{32 a r_{ij}}\right] & \text{for } i \neq j \text{ and } r_{ij} < 2a. \end{cases} \tag{8}$$

Here, a is the hydrodynamic radius of each bead, which is approximately taken as the bead diameter σ, and η is the solvent viscosity, which is related to the drag coefficient by the relation $\beta = 6\pi\eta a$. With the above description of the solvent flow, we solve the Langevin equation in the overdamped limit and use the following stochastic differential equation for each bead:

$$d\mathbf{r}_i = \left(\nabla\mathbf{u}\cdot\mathbf{r}_i + \sum_{j=1}^{N}\frac{\mathbf{D}_{ij}\cdot\mathbf{F}_j}{k_B T}\right)dt + \sqrt{2dt}\sum_{j=1}^{i}\boldsymbol{\alpha}_{ij}\cdot\mathbf{G}_j. \tag{9}$$

Here, $\nabla\mathbf{u}$ is the previously defined velocity gradient tensor, and $\mathbf{F}$ is the net force on a polymer bead, including the active force as defined in the equations 3 and 4. $\mathbf{G}$ is a random Gaussian vector with zero mean and unit variance. The elements of $\mathbf{D}$ are positive definite by construction, which allows the Cholesky decomposition given by $\mathbf{D} = \boldsymbol{\alpha}\cdot\boldsymbol{\alpha}^T$. Previous works on passive polymers[1, 3] have shown a faster relaxation in the presence of HI, which we recover in our case as well. For a passive ring polymer with $N = 100$, simulations in the absence of shear flow ($\dot{\gamma}$) indicate that the polymer relaxation is faster when hydrodynamic interaction is considered. We find the relaxation time for the passive polymer to be $\tau_0^{HI+} \approx 1200$ with HI, while $\tau_0^{HI-} \approx 5000$ without HI.

To test the effect of HI on the ability of shear to distinguish the two activities, we plot the probability distribution $P(R_g)$ in Fig. S18 with and without HI for $N = 100$ and $Wi = 600$. In this Wi regime, the polymer prefers to be in the open state. Fig. S18 reveals that both in the presence and absence of HI, the type-II activity possesses finite weight for lower Rgs, which is not the case with type-I activity. That is, the probability values for smaller R_g increase at the cost of probability values at higher R_g. This indicates that, again, in the presence of HI, the type-I active ring has fewer fluctuations in the open state than type-II.

The stalling or slowing down of the tank-treading motion in the type-I active ring is also found to be consistent in the presence of HI. Fig S19 shows the time-series of x_i/L for $Ac\text{-}I = 10$ and $Ac\text{-}II = 10$ at two different Wi. At $Wi = 600$, the TT motion in both type-I and type-II active rings are similar (Fig.S19a). However, upon increasing Wi to 1200, the frequency of oscillation in x_i/L increased for type-II, whereas it decreased drastically in the type-I ring. This again indicates the stalling of TT motion as observed before without HI. Therefore, the stalling is purely related to the activity, where tank-treading due to shear tries to balance the tank-treading due to activity.

It must be noted that though the results after the inclusion of HI match qualitatively with previous results without HI, the values of Wi, where we observe closed and open states in

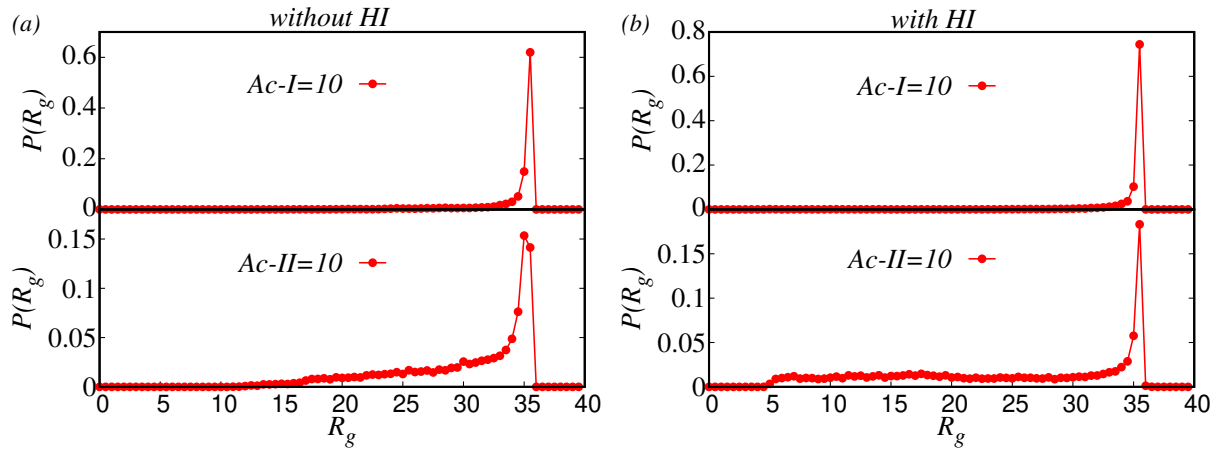

Figure S18: Distribution of R_g at $Wi = 600$ of a ring polymer with a degree of polymerization $N = 100$ with $Ac\text{-}I, II = 10$, (a) without HI and (b) with HI. Note that for type-II activity, the peak height of the distribution decreases and probability values at smaller R_g increase with respect to type-I. The difference between type-I and type-II activities persists both in the absence and presence of HI.

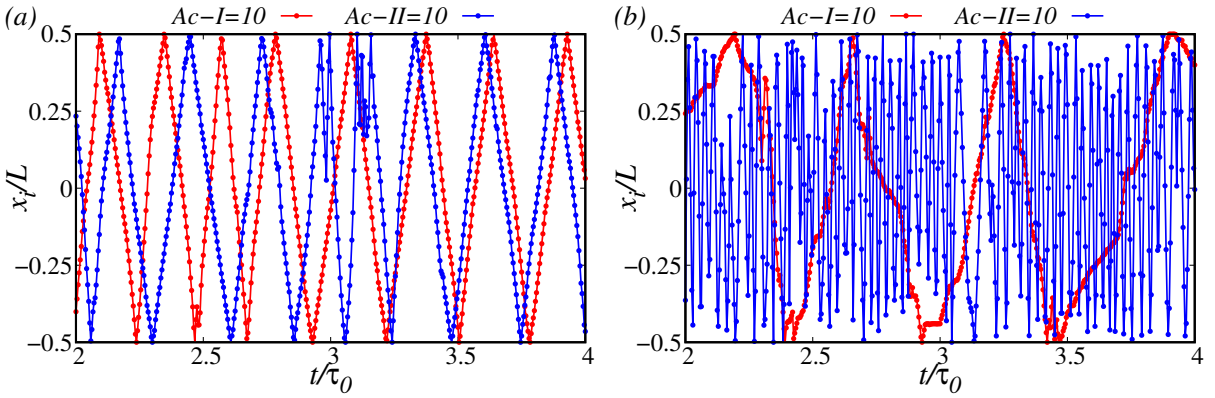

Figure S19: Variation of x_i/L of the $N = 100$ active ring at (a) $Wi = 600$ and (b) $Wi = 1200$.

the ring, are different. We observe that the shear rate required to open the active polymer from its closed state is higher in the presence of HI.

Our claim is only that both activities can be differentiated by applying a shear flow to the active chromatin polymer. Whether with HI or without HI, it is clear that the polymer will transition from a closed to an open state and exhibit different behaviour as a function of Wi. For our conclusion, the precise value of Wi does not matter; what matters is only the appearance of distinct behaviour as we vary the parameters.

S6 Effect of non-uniform active force

The molecular motors acting on chromatin may have some diversity/stochasticity in terms of their activity strength. To address this issue, we separately model an active loop polymer system where the motor activity (type-I or type-II) is taken to be non-uniform. To bring this non-uniformity we sample f_t of equation 3 and 4 from a uniform distribution such that $Ac \in [9, 11]$ with mean $Ac = 10$. We compare the R_g distribution of this motor-chromatin system with $Ac\text{-}I = 10$ and $Ac\text{-}II = 10$ in Fig. S20. It is evident that even in the presence

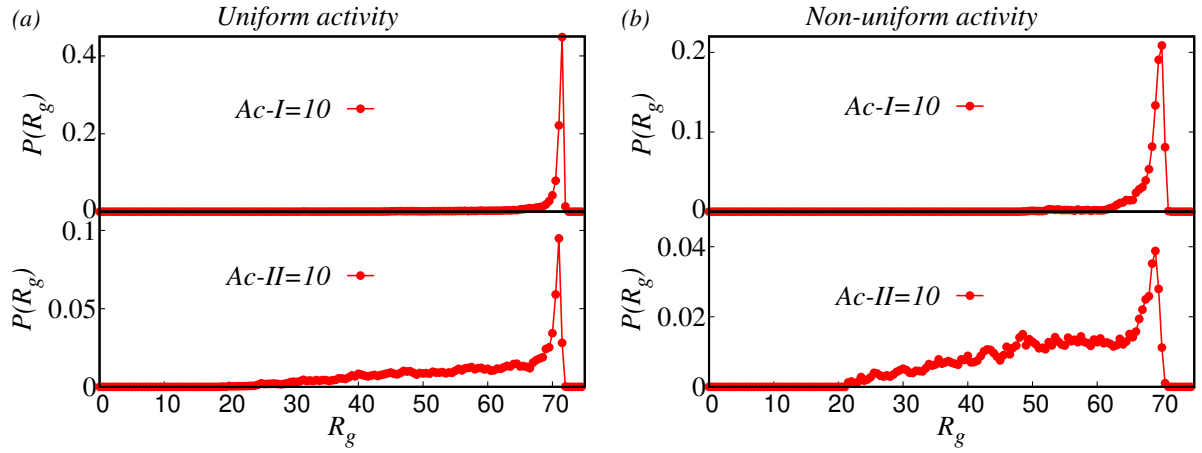

Figure S20: Distribution of R_g at $Wi = 75$ with stochastic active force, for $Ac\text{-}I, II = 10$. Just like in the uniform activity case, the difference between type-I and type-II activities persists even with non-uniform activity.

of non-uniform forcing of motors, the type-I and type-II activities retain their features. In fact, the non-uniformity enhances the difference between the two types. The type-I activity is roughly as open as before, whereas type-II becomes more deformable in the open state. Just like in the uniform activity case, the difference between type-I and type-II activities persists even with non-uniform activity.

S7 Movie Description

- **Movie 1** (movie1.mp4): Tumbling motion in type-II active ring at $Wi = 370$ and $Ac\text{-}II = 10$.
- **Movie 2** (movie2.mp4): Pure tank-treading motion of type-I active ring at $Wi = 370$ and $Ac\text{-}I = 10$. For clear visualization of TT motion, a small segment of the ring has been marked in red colour.
- **Movie 3** (movie3.mp4): Stalling of type-I active ring at $Wi = 7500$ and $Ac\text{-}I = 10$.
- **Movie 4** (movie4.mp4): Type-II active ring showing a mix of tumbling and tank-treading dynamics at $Wi = 7500$ and $Ac\text{-}II = 10$.

References

[1] N Kikuchi, A Gent, and JM Yeomans. "Polymer collapse in the presence of hydrodynamic interactions". In: *The European Physical Journal E* 9 (2002), pp. 63–66.

[2] Sandeep Kumar and Snigdha Thakur. "Local Polar and Long-Range Isotropic Activity Assisted Swelling and Collapse Dynamics of an Active Ring Polymer". In: *Macromolecules* 56.14 (2023), pp. 5229–5236.

[3] Tri Thanh Pham, Mohit Bajaj, and J Ravi Prakash. "Brownian dynamics simulation of polymer collapse in a poor solvent: Influence of implicit hydrodynamic interactions". In: *Soft Matter* 4.6 (2008), pp. 1196–1207.

[4] Michael Q. Tu et al. "Direct Observation of Ring Polymer Dynamics in the Flow-Gradient Plane of Shear Flow". In: *Macromolecules* 53.21 (2020), pp. 9406–9419. DOI: 10.1021/acs.macromol.0c01362. eprint: https://doi.org/10.1021/acs.macromol.0c01362. URL: https://doi.org/10.1021/acs.macromol.0c01362.

[5] Charles D Young et al. "Ring polymer dynamics and tumbling-stretch transitions in planar mixed flows". In: *Physical Review E* 99.6 (2019), p. 062502.